

A hemispherical dynamo model : Implications for the Martian crustal magnetization

Wieland Dietrich^{1,2} & Johannes Wicht²

²Max-Planck-Institut für Sonnensystemforschung,
Max-Planck-Strasse 2, 37191 Katlenburg-Lindau, Germany

¹Institute for Geophysics,
University of Göttingen, 37073 Göttingen, Germany

May 24, 2022

Mars Global Surveyor measurements revealed that the Martian crust is strongly magnetized in the southern hemisphere while the northern hemisphere is virtually void of magnetization. Two possible reasons have been suggested for this dichotomy: A once more or less homogeneous magnetization may have been destroyed in the northern hemisphere by, for example, resurfacing or impacts. The alternative theory we further explore here assumes that the dynamo itself produced a hemispherical field [Stanley et al., 2008, Amit et al., 2011]. We use numerical dynamo simulations to study under which conditions a spatial variation of the heat flux through the core-mantle boundary (CMB) may yield a strongly hemispherical surface field. We assume that the early Martian dynamo was exclusively driven by secular cooling and we mostly concentrate on a cosine CMB heat flux pattern with a minimum at the north pole, possibly caused by the impacts responsible for the northern lowlands. This pattern consistently triggers a convective mode which is dominated by equatorially anti-symmetric and axisymmetric (EAA, Landeau and Aubert [2011]) thermal winds. Convective up- and down-wellings and thus radial magnetic field production then tend to concentrate in the southern hemisphere which is still cooled efficiently while the northern hemisphere remains hot. The dynamo changes from an α^2 - for a homogeneous CMB heat flux to an $\alpha\Omega$ -type in the hemispherical configuration. These dynamos reverse on time scales of about 10 kyrs. This too fast to allow for the more or less unidirectional magnetization of thick crustal layer required to explain the strong magnetization in the southern hemisphere.

1 Introduction

Starting in 1998 the space probe Mars Global Surveyor (MGS) delivered vector magnetic field data from orbits between 185 and 400 km above the planets surface [Acuña et al., 1999]. The measurements reveal a strong but heterogeneous crustal magnetization [Acuña et al., 1999, Connerney et al., 2001]. The more strongly magnetized rocks are mainly localized in the southern hemisphere where the crust is thick and old. The northern hemisphere is covered by a younger and thinner crust which is much weaker magnetized.

Two alternative types of scenarios are discussed to explain this dichotomy. One type explores the possibility that an originally more or less homogeneous magnetization was partly destroyed by resurfacing events after the demise of the internal dynamo. Based on the fact that the Hellas and Argyre impact basins are largely void of magnetization, Acuña et al. [2001] conclude that the dynamo stopped operating in the early Noachian before the related impact events happened roughly 3.7–4 Gyrs ago. Volcanic activity and crustal spreading are two other possibilities to explain the lack of strong magnetization in certain surface areas [Lillis et al., 2008, Mohit and Arkani-Hamed, 2004], in particular the northern hemisphere after the dynamo cessation.

The alternative scenario explains the dichotomy by an ancient Martian dynamo that inherently produced a hemispherical magnetic field. Numerical dynamo simulations by Stanley et al. [2008] and Amit et al. [2011] show that this may happen when more heat is allowed to escape the core through the southern than through the northern core mantle boundary (CMB). Such north/south asymmetry can for example be caused by larger impacts or low-degree mantle convection [Roberts and Zhong, 2006, Keller and Tackley, 2009, Yoshida and Kageyama, 2006]. Due to depth-dependent viscosity and a possible endothermic phase transition [Harder and Christensen, 1996] Martian mantle convection may be ruled in an extreme case by one gigantic plume typically evoked to explain the dominance of the volcanic Tharsis region. However, the single plume convection might have developed after the dynamo ceased. Due to the hotter temperature of the rising material the CMB heat flux can be significantly reduced under such a plume. Though Tharsis is roughly located in the equatorial region it could nevertheless lead to magnetic field with the observed north-south symmetry, as we will show in the following.

The possible effects of large impacts on planets and the dynamo in particular are little understood. Roberts et al. [2009] argue that impacts locally heat the underlying mantle and thereby lead to variations in the CMB heat flux. Large impacts may also cause a demise of the dynamo by reducing the CMB heat flux below the value where subcritical dynamo action is still possible [Roberts et al., 2009]. The deposition of heat in the outer parts of the core by impact shock waves could lead to a stably stratified core and thereby also stop dynamo action [Arkani-Hamed and Olson, 2010] for millions of years until the heat has diffused out of the core. If the iron content of the impactor is large enough it may even trigger a dynamo [Reese and Solomatov, 2010].

The thermal state of the ancient Martian core is rather unconstrained [Breuer et al., 2010]. Analysis of Martian meteorites suggests a significant sulphur content and thus a high core melting temperature [Dreibus and Wänke, 1985]. Mars may therefore never

44 have grown a solid inner core, an assumption we also adopt here [Schubert and Spohn,
 45 1990, Breuer et al., 2010]. The ancient Martian dynamo was then exclusively driven
 46 by secular cooling and radiogenic heating and has stopped operating when the CMB
 47 heat flux became subadiabatic [Stevenson et al., 1983]. Run-away solidification or light
 48 element saturation may explain the dynamo cessation in the presence an inner core.

49 The geodynamo, on the other hand, is predominantly driven by the latent heat and
 50 light elements emanating from the growing inner core front. Secular cooling and ra-
 51 diogenic heating is typically modeled by homogeneously distributed internal buoyancy
 52 sources while the driving associated to inner core growth is modeled by bottom sources
 53 [Kutzner and Christensen, 2000]. These latter sources have a higher Carnot efficiency
 54 and would likely have kept the Martian dynamo alive if the planet would have formed
 55 an inner core.

56 Several authors have explored the influence of a CMB heat flux pattern on dynamos
 57 geared to model Earth and report that they can cause hemispherical variations in the
 58 secular variation [Bloxham, 2000, Christensen and Olson, 2003, Amit and Olson, 2006],
 59 influence the reversal behavior [Glatzmaier et al., 1999, Kutzner and Christensen, 2004]
 60 or lead to inhomogeneous inner core growth [Aubert et al., 2008]. However, the effects
 61 where never as drastic as those reported by Stanley et al. [2008] or Amit et al. [2011]. In
 62 the work of Amit et al. [2011] the reason likely is the increased susceptibility of internally
 63 driven dynamos to the thermal CMB boundary condition [Hori et al., 2010]. Stanley
 64 et al. [2008] retain bottom driving and employed a particularly strong heat flux variation
 65 to enforce a hemispherical field

66 Here, we follow Amit et al. [2011] in exploring the effects of a simple sinusoidal CMB
 67 heat flux variation on a dynamo model driven by internal heat sources. The main scope
 68 of this paper is to understand the particular dynamo mechanism, to explore its time
 69 dependence, and to extrapolate the results to the Martian situation. Section 2 introduces
 70 our model, whereas section 3 describes the effects of the CMB heat flux anomaly on the
 71 convection and the induction process. In section 4 we explore the applicability to the
 72 ancient Martian dynamo. The paper closes with a discussion in section 5.

73 2 Numerical Model

74 Using the MagIC code [Wicht, 2002, Christensen et al., 2007], we model the Martian
 75 core as a viscous, electrically conducting and incompressible fluid contained in a rotat-
 76 ing spherical shell with inner core radius r_{icb} and outer radius r_{cmb} . Conservation of
 77 momentum is described by the dimensionless Navier-Stokes equation for a Boussinesq
 78 fluid:

$$E \left(\frac{\partial \vec{u}}{\partial t} + \vec{u} \cdot \vec{\nabla} \vec{u} \right) = -\vec{\nabla} \Pi + E \nabla^2 \vec{u} - 2\hat{z} \times \vec{u} + \frac{RaE}{Pr} \frac{\vec{r}}{r_{cmb}} T + \frac{1}{Pm} (\vec{\nabla} \times \vec{B}) \times \vec{B} \quad (1)$$

79 where \vec{u} is the velocity field, Π the generalized pressure, \hat{z} the direction of the rotation
 80 axis, T the super-adiabatic temperature and \vec{B} the magnetic field.

81 The conservation of energy is given by

$$\frac{\partial T}{\partial t} + \vec{u} \cdot \vec{\nabla} T = \frac{1}{Pr} \nabla^2 T + \epsilon, \quad (2)$$

82 where ϵ is a uniform heat source density. The conservation of magnetic field is given by
83 the induction equation

$$\frac{\partial \vec{B}}{\partial t} = \vec{\nabla} \times (\vec{u} \times \vec{B}) + \frac{1}{Pm} \nabla^2 \vec{B}. \quad (3)$$

84 We use the shell thickness $D = r_{cmb} - r_{icb}$ as length scale, the viscous diffusion time
85 D^2/ν as time scale and $(\rho\mu\lambda\Omega)^{1/2}$ as the magnetic scale. The mean superadiabatic
86 CMB heat flux density q_0 serves to define the temperature scale $q_0 D/c_p \rho \kappa$. Here, ν is
87 the viscous diffusivity, ρ the constant background density, μ the magnetic permeability,
88 λ the magnetic diffusivity, Ω the rotation rate, κ the thermal diffusivity and c_p the heat
89 capacity.

90 Three dimensionless parameters appear in the above system: the Ekman number
91 $E = \nu/\Omega D^2$ is a measure for the relative importance of viscous versus Coriolis forces
92 while the flux based Rayleigh number $Ra = \alpha g_0 |q_0| D^4 / \rho c_p \kappa^2 \nu$ is a measure for the
93 importance of buoyancy. The Prandtl number $P = \nu/\kappa$ and the magnetic Prandtl
94 number $Pm = \nu/\lambda$ are diffusivity ratios.

An inner core with $r_{icb}/r_{cmb} = 0.35$ is retained for numerical reasons [Hori et al., 2010], but to minimize its influence the heat flux from the inner core is set to zero. The secular cooling and radiogenic driving is modeled by the homogeneous heat sources ϵ appearing in 2 [Kutzner and Christensen, 2000]. Furthermore we assume an electrically insulating inner core to avoid an additional sink for the magnetic field. We use no-slip, impermeable flow boundary conditions and match \vec{B} to a potential field at the outer and inner boundary. The results by Hori et al. [2010] and Aubert et al. [2009] suggest that this is a fair approximation to model a dynamo without inner core since an additional reduction of the inner core radius has only a minor impact. The effective heat source ϵ is chosen to balance the mean heat flux q_0 through the outer boundary:

$$4\pi^2 r_{cmb}^2 q_0 = -Pr \frac{4}{3} \pi (r_{cmb}^3 - r_{icb}^3) \epsilon. \quad (4)$$

Note that q_0 is generally negative. The CMB heat flux pattern is modeled in terms of spherical harmonic contributions with amplitude q_{lm} , where l is the degree and m the spherical harmonic order. Here we mostly concentrate on a variation along colatitude ϑ of the form $q_{10} \cos \vartheta$ with negative q_{10} so that the minimum (maximum) heat flux is located at the north (south) pole. This is the most simple pattern to break the north/south symmetry and has first been used by Stanley et al. [2008] in the context of Mars. We also explore the equatorially symmetric disturbance $q_{11} \sin \vartheta \sin \phi$, which breaks the east/west symmetry, and a superposition of q_{10} and q_{11} to describe a cosine

disturbance with arbitrary tilt angle

$$\alpha = \arctan(|q_{11}|/|q_{10}|) . \quad (5)$$

In the following we will characterize the amplitude of any disturbance by its maximum relative variation amplitude in percent

$$g = 100\% \max(|\delta q|)/|q_0| . \quad (6)$$

95 We vary g up to 300%, the value used in [Stanley et al. \[2008\]](#). For variations beyond
 96 100% the heat flux becomes subadiabatic in the vicinity of the lowest flux. For severely
 97 subadiabatic cases this may pose a problem since dynamo codes typically solve for small
 98 disturbances around an adiabatic background state [[Braginsky and Roberts, 1995](#)]. The
 99 possible implication of this have not been explored so far and we simply assume that
 100 the model is still valid. Since the main effects described below do not rely on $g > 100\%$
 101 this is not really an issue here.

The hemispherical mode triggered by the heat flux variation is dominated by equatorially anti-symmetric and axisymmetric thermal winds [[Landeau and Aubert, 2011](#)]. Classical columnar convection found for a homogeneous heat flux, on the other hand, is predominantly equatorial symmetric and non-axisymmetric, at least at lower Rayleigh numbers. We thus use the relative equatorial anti-symmetric and axisymmetric (EAA) kinetic energy to identify the hemispherical mode:

$$\mathcal{A} = \frac{\sum_{l_{\text{odd}}, m=0} E_{lm}}{\sum_{lm} E_{lm}} , \quad (7)$$

102 where E_{lm} is the rms kinetic energy carried by a flow mode of spherical harmonic degree
 103 l and order m .

104 For a homogeneous outer boundary heat flux the dynamo is to first order of an α^2 -
 105 type where poloidal and toroidal fields are produced in the individual convective columns
 106 [[Olson et al., 1999](#)]. As the hemispherical flow mode takes over, the Ω -effect representing
 107 the induction of axisymmetric toroidal magnetic field via axisymmetric shearing becomes
 108 increasingly important. We measure its relative contribution to toroidal field production
 109 by

$$\mathcal{O} = \frac{\left[(\vec{B} \cdot \vec{\nabla}) \bar{u}_\phi \right]_{\text{tor}}^{\text{rms}}}{\left[(\vec{B} \cdot \vec{\nabla}) \bar{u} \right]_{\text{tor}}^{\text{rms}}} . \quad (8)$$

110 The lower index tor and upper index rms indicate that rms values of the toroidal field
 111 production in the shell are considered.

112 For quantifying to which degree the Martian crustal magnetization and the poloidal
 113 magnetic fields in our dynamo simulations are concentrated in one hemisphere we use
 114 the hemisphericity measure

$$\mathcal{H}(r) = \left| \frac{B_r^N(r) - B_r^S(r)}{B_r^N(r) + B_r^S(r)} \right| , \quad (9)$$

115 where $B_r^N(r)$ and $B_r^S(r)$ are the surface integral over the unsigned radial magnetic flux in
116 the northern and southern hemispheres, respectively. According to this definition both
117 a purely equatorially symmetric and a purely equatorially anti-symmetric field yield
118 $\mathcal{H} = 0$. For $\mathcal{H} = 1$ the flux is strictly concentrated in one hemisphere which requires a
119 suitable combination of equatorially symmetric and anti-symmetric modes [Grote and
120 Busse, 2000]. A potential field extrapolation is used to calculate \mathcal{H} for radii above r_{cmb} ,
121 for example the surface hemisphericity \mathcal{H}_{sur} .

122 Table 1 provides an overview of the different parameter combinations explored in this
123 study along with \mathcal{A} , \mathcal{O} , \mathcal{H}_{cmb} , \mathcal{H}_{sur} , the Elsasser number $\Lambda = B^2/\mu_0\lambda\rho\Omega$ and the field
124 strength at the Martian surface in nano Tesla \bar{B}_{sur} . Column 14 lists the respective (if
125 present) dimensionless oscillation frequencies given in units of magnetic diffusion time.

126 We mostly focus on simulations at $E = 10^{-4}$ where the relatively moderate numer-
127 ical resolution still allows to extensively explore the other parameters in the system.
128 A few cases at $E = 3 \times 10^{-5}$ and $E = 10^{-5}$ provide a first idea of the Ekman num-
129 ber dependence. The last line in table 1 gives estimates for the Rayleigh, Ekman and
130 magnetic Prandtl number of Mars, based on the (rather uncertain) properties of Mars
131 [Morschhauser et al., 2011].

E	Ra	Pm	g	α	Rm	Rm^*	Λ	\mathcal{A}	\mathcal{O}	\bar{B}_{sur}	\mathcal{H}_{sur}	\mathcal{H}_{cmb}	freq.
1e-4	7e6	2	0	0	54.6	0.24	-	2.24e-5	-	-	-	-	-
			100	0	133.5	122.6	0.1	0.85	0.32	803.2	0.1	0.21	-
		5	0	0	117.1	3.95	9.79	1.93e-3	0.21	62510	4e-4	3e-3	-
			100	0	326.9	301.5	0.97	0.85	0.66	1469	0.1	0.35	?
			200	0	449.5	417.5	-	0.84	-	-	-	-	-
100	90	230.8	-	2.22	5e-3	0.20	7264	-	-	-	18.84		
2.1e7	2	0	0	105.9	6.42	4.95	3.64e-3	0.24	64635	1.0e-3	0.03	-	
		60	0	178.1	149.8	6.24	0.72	0.63	14017	0.12	0.38	-	
		80	0	228.3	189.7	1.06	0.74	0.53	1684	0.17	0.61	10.69	
		100	0	247.6	213.6	0.15	0.73	0.58	1001	0.21	0.55	?	
		200	0	313.3	272	0.19	0.76	0.77	689	0.79	0.8	56.27	
100	90	160.2	-	2.64	6.6e-3	0.18	699	-	-	-	?		
4e7	1	100	0	169.3	143.1	0.2	0.73	0.53	922	0.21	0.22	-	
		200	0	206.5	171.5	-	0.7	-	-	-	-	-	?
	2	0	0	155.6	3.58	6.26	2e-3	0.18	58349	3.0e-3	0.05	-	
		60	0	283.4	252.4	4.18	0.59	0.65	6154	0.26	0.6	13.96	
		100	0	338.1	307.2	2.64	0.78	0.76	2219	0.52	0.77	40.83	
		200	0	409.8	350	1.16	0.74	0.75	1628	0.74	0.75	62.6	
		100	90	217.3	-	1.47	8.4e-3	0.21	10071	-	-	20.77	
		200	90	226.5	-	5.41	4.1e-3	0.24	10934	-	-	-	
	5	100	0	837.5	749.5	6.83	0.81	0.8	3493	0.7	0.65	79.87	
	8e7	2	0	0	228.7	6.4	7.06	9e-3	0.18	60036	3.3e-3	0.07	-
60			0	400.2	343.6	5.5	0.74	0.65	9268	0.41	0.72	26.97	
100			0	457.6	403.2	2.97	0.79	0.73	3240	0.68	0.73	61.3	
100			90	297.5	-	3.73	6.4e-3	0.20	16424	-	-	24.5	
2e8	1	0	0	251.8	54.4	-	0.05	-	0	-	-	-	
		60	0	309.9	230.1	2.14	0.63	0.56	6095	0.15	0.56	-	
		100	0	343.5	276.3	0.34	0.64	0.65	1119	0.42	0.72	24.32	
		100	90	270.4	-	0.77	4e-3	0.21	7954	-	-	17.95	
3e-5	1e8	2	0	0	137.1	2.88	7.68	5.7e-3	0.19	80508	1e-3	0.03	-
			60	0	210.7	48.2	12.31	0.5	0.53	25567	0.1	0.23	-

			100	0	360.4	324.2	5.07	0.81	0.67	5157	0.12	0.46	10.34
			100	90	199.5	-	1.4	3.1e-3	0.16	10657	-	-	?
3e-5	4e8	2	0	0	316.9	6.62	12.2	5.5e-3	0.26	71085	2.1e-3	0.07	-
			60	0	517.1	401.8	29.9	0.64	0.49	30528	0.24	0.51	-
			100	0	769.1	682	6.04	0.76	0.70	4584	0.62	0.76	87.6
1e-5	4e8	2	0	0	234.9	586	13.58	0.01	0.18	88763	6e-3	0.09	-
			50	0	292.5	146.2	19.07	0.18	0.23	69618	0.03	0.22	-
			100	0	441.1	376.4	41.7	0.41	0.26	42194	0.07	0.30	-
Mars													
3e-15	2e28	1e-6	?	?	500?	?	?	?	?	5000	0.45	?	?

Table 1: Selection of runs performed. Rm - magnetic Reynolds number, Λ - Elsasser number of rms field in full core shell, EAA - relative equatorially antisymmetric and axisymmetric kinetic energy, ω^* - relative induction of toroidal field by shearing, $|B|_{sur}$ - time averaged field intensity at the Martian surface, \mathcal{H}_{sur} and \mathcal{H}_{cmb} - hemisphericity at the surface and CMB, freq. - rough frequency ($2\pi Pm/\tau_{vis}$) if present. Decaying solutions are marked with ‘-’ in the Elsasser number, stationary dynamos with ‘-’ in the frequency. If not a single frequency could be extracted ‘?’ is used.

132 3 Hemispherical Solution

133 We start with discussing the emerging hemispherical dynamo mode promoted by the
134 $l = 1, m = 0$ heat flux pattern with minimal (maximal) heat flux at the north (south)
135 pole concentrating on cases at $E = 10^{-4}$, $Ra = 4.0 \times 10^7$ and $Pm = 2$. The study of
136 [Landeau and Aubert \[2011\]](#) reports the emergence of the equatorially anti-symmetric
137 and axisymmetric convective mode if the Rayleigh number is sufficiently high. Note,
138 that the authors used a homogeneous heat flux condition at the outer boundary. There
139 the amplitude of the hemispherical convection becomes of equal strength compared to
140 the columnar type in the pure hydrodynamic case and is even more dominant if the
141 magnetic field can act on the flow [[Landeau and Aubert, 2011](#)].

142 3.1 Hemispherical Convection

143 Figure 1 and 2 illustrate the typical hemispherical dynamo configuration emerging at
144 $g = 100\%$ and compares this with the typical dipole dominated dynamo found at $g = 0\%$.
145 While the southern hemisphere is still cooled efficiently the northern hemisphere remains
146 hot since radial upwellings and the associated convective cooling are predominantly con-
147 centrated in the southern hemisphere (figure 2, top row). The flow pattern changes from
148 classical columnar solutions to a thermal wind dominated flow which is a direct conse-
149 quence of the strong north/south temperature gradient (figure 1, left bottom). When
150 neglecting inertial, viscous and Lorentz force contributions the azimuthal component of
151 the curl of the Navier-Stokes equation (1) yields:

$$2 \frac{\partial \bar{u}_\phi}{\partial z} = \frac{RaE}{Pr} \frac{1}{r_{cmb}} \frac{\partial \bar{T}}{\partial \vartheta} . \quad (10)$$

152 This is the thermal wind equation and the respective zonal flows will dominate the
 153 solution, indicated by large \mathcal{A} values when the latitudinal temperature gradient is large
 154 enough [Landeau and Aubert, 2011]. Since radial flows mainly exist in the southern
 155 hemisphere the production of poloidal and thus radial magnetic field is also concentrated
 156 there. This results in a very hemispherical magnetic field pattern at the top of the
 157 dynamo region (figure 2, bottom row).

158 The figure 3 demonstrates that the toroidal energy rises quickly with the variation
 159 amplitude g while the poloidal energy is much less effected. The growth of the toroidal
 160 energy is explained by the increasing thermal wind, which is an equatorial anti-symmetric
 161 and axisymmetric (EAA) toroidal flow contribution. At a disturbance amplitude of
 162 $g = 60\%$ the EAA contribution accounts for already 50% of the total kinetic energy
 163 (figure 3.b). The maximum EAA contribution of $\mathcal{A} \approx 0.8$ is reached at $g = 100\%$.
 164 When further increasing the variation amplitude, the thermal wind still gains in speed.
 165 However, the relative importance of the EAA mode decreases because the strongest
 166 latitudinal temperature gradient and thus the thermal wind structure moves further
 167 south. This trend is already observed in figure 1.

168 The equatorial anti-symmetry of the poloidal kinetic energy rises from 10% for $g = 0$
 169 to about 50% for $g = 100\%$ reflecting that upwellings are increasingly concentrated in
 170 one (southern) hemisphere. The meridional circulation remains weak (figure 3.d), and
 171 its contribution to the total EAA energy is minor.

172 3.2 Dynamo mechanism

173 The upper panel in figure 4 demonstrates that the rise in the magnetic Reynolds number
 174 Rm , that goes along with the increasing toroidal flow amplitude, does not necessarily
 175 lead to higher Elsasser numbers. Once more, cases at $E = 10^{-4}$, $Ra = 4.0 \times 10^7$ and
 176 $Pm = 2$ are depicted here. For small variation amplitudes up to $g = 30\%$ Λ still increases
 177 due to the additional Ω -effect associated to the growing thermal winds. Figure 4 (lower
 178 panel) shows that the relative contribution of the Ω -effect to toroidal field production
 179 \mathcal{O} grows with g . For $g = 0$ it is rather weak so that the dynamo can be classified as α^2
 180 [Olson et al., 1999]. Around $g = 50\%$, \mathcal{O} reaches 50% and the dynamo is thus of an $\alpha^2\Omega$ -
 181 type. When increasing g further the classical convective columns practically vanish and
 182 the associated α -effects decrease significantly, leading to both weak poloidal and toroidal
 183 fields (figure 4, lower panel). For the toroidal field the effect is somewhat compensated
 184 by the growing Ω -effect. The hemispherical dynamo clearly is an $\alpha\Omega$ -dynamo.

185 At $g = 100\%$ the hemispherical mode clearly dominates and the dynamo is of the
 186 $\alpha\Omega$ -type with $\mathcal{O} \approx 0.8$. The Elsasser number has dropped to half its value at $g = 0$ while
 187 the magnetic Reynolds number has increased by a factor two (figure 4, upper panel).
 188 The hemispherical dynamo is clearly less effective than the columnar dynamo.

189 Figure 5 illustrates the hemispherical dynamo mechanism in a 3D rendering. Magnetic
 190 field lines show the magnetic field configuration, their thickness is scaled with the local
 191 magnetic energy while red and blue colors intensities indicate the relative inward and
 192 outward radial field contribution. Plain gray lines are purely horizontal. Red and blue
 193 isosurfaces characterize inward and outward directed radial plume-like motions produc-

194 ing radial field magnetic field. Strong axisymmetric zonal field is produced by a thermal
195 wind related Ω -effect around the equatorial plane.

196 3.3 Magnetic Oscillations

197 Figure 6 illustrates the changes in the time behavior of the poloidal magnetic field when
198 the CMB heat flux variation is increased. We concentrate on axisymmetric Gaussian
199 coefficients at the CMB ($r = r_{cmb}$) here. In the reference case $g = 0$ (top panel) the
200 axial dipole dominates, varies chaotically in time and never reverses. If g is increased
201 to 50% (second panel) the relative importance of the axial quadrupole component has
202 increased significantly, which indicates the increasing hemisphericity of the magnetic
203 field. To yield a hemispherical magnetic field a similar amplitude in dipolar (equatorial
204 antisymmetric) and quadrupolar (equatorial symmetric) dynamo family contributions is
205 required [Landeau and Aubert, 2011, Grote and Busse, 2000].

206 When increasing the variation slightly to $g = 60\%$ (third panel) where the hemi-
207 spherical mode finally dominates, all coefficients assume a comparable amplitude and
208 oscillate in phase around a zero mean with a period of roughly half a magnetic diffusion
209 time. The faster convective flow variations can still be discerned as a smaller amplitude
210 superposition in figure 6.

211 The oscillation is also present in a kinematic simulation performed for comparison and
212 is thus a purely magnetic phenomenon. Lorentz forces nevertheless cause the flow to
213 vary along with the magnetic field. Since the coefficients vary in phase there are times
214 where the magnetic field and thus the Lorentz forces are particularly weak or particularly
215 strong. Figure 7 illustrates the solutions at maximum (top) and minimum (middle) rms
216 field strength. At the minimum the convective columns are still clearly present and the
217 flow is similar to that found in the non-magnetic simulations shown in the lower panel
218 of figure 7. At the maximum the Lorentz forces, in particular those associated with the
219 strong zonal toroidal field, severely suppress the columns. The magnetic field thereby
220 further promotes the dominance of the hemispherical mode [Landeau and Aubert, 2011].
221 This becomes even more apparent when comparing the relative importance of the EAA
222 mode \mathcal{A} in magnetic and non-magnetic simulations in the top panel of figure 8. In the
223 dynamo run \mathcal{A} is around 35% higher than in the non-magnetic case for mild heat flux
224 variation amplitudes.

225 When further increasing the amplitude of the CMB heat flux pattern, the frequency
226 grows, the time behavior becomes somewhat more complex, and the different harmonics
227 vary increasingly out of phase. In addition, the relative importance of harmonics higher
228 than the dipole increase which indicates a concentration of the field at higher southern
229 latitudes. The impact of the oscillations on the flows decreases since the hemispherical
230 mode now always clearly dominates and the relative variation in the magnetic field
231 amplitude becomes smaller.

232 The appearance of the oscillations may result from the increased importance of the
233 Ω -effect which at $g = 60\%$ starts to dominate toroidal field production (see figure 4,
234 lower panel). The Ω -effect could be responsible for the oscillatory behavior of the so-
235 lar dynamo as has, for example, been demonstrated by Parker [1955] who describes

236 a simple purely magnetic wave phenomenon. [Busse and Simitev \[2006\]](#) report Parker
237 wave type oscillatory behavior in their numerical dynamo simulations where the stress
238 free mechanical boundary conditions promote strong zonal flows and thus a significant
239 Ω -effect.

240 3.4 Arbitrary tilt angle

241 To explore to which degree the effects described above still hold when the variation and
242 rotation axis do not coincide we systematically vary the variation pattern tilt angle α
243 (see eq. 5) up to 90 degrees. The lower panel in figure 8 shows how \mathcal{A} , the relative
244 EAA kinetic energy, varies with g for different tilt angles. Somewhat surprisingly, the
245 hemispherical mode still clearly dominates for tilt angles up to $\alpha = 80^\circ$. Only the rather
246 special case of $\alpha = 90^\circ$ shows a new behavior, where \mathcal{A} remains negligible. It is thus
247 the general breaking of the north/south symmetry that is essential here. Since it leaves
248 the northern hemisphere hotter than the southern it always leads to the above described
249 dynamo mode.

250 The 90 degree tilt angle of the ($l = 1, m = 1$) pattern forms a special case because
251 the breaking of the north-south symmetry is missing here. Finally, the effects of the
252 east/west symmetry breaking become apparent and supersede the thermal wind related
253 action in the other cases. Figures 9 and 10 illustrate the solution for an equatorial
254 anomaly with $g = 200\%$.

255 The resulting east/west temperature difference drives a large scale westward directed
256 flow and a more confined eastward flow in the equatorial region of the outer part of the
257 shell (figure 9). Coriolis forces divert the westward directed flow poleward and inward,
258 and lead to the confinement of the eastward directed flow. Consequently, the westward
259 flow plays the more important role here.

260 The diverted flows feed two distinct downwelling features that form at the latitude
261 of zero heat flux disturbance close to the tangent cylinder. Due to the significant time
262 dependence of the solution these can best be identified in time average flows shown in
263 figure 10. Convective columns concentrated in the high heat flux hemisphere but the
264 center of their action is somewhat shifted retrograde, probably due to the action of
265 azimuthal winds. Other authors have shown that this shift, for example, depends on
266 the Ekman number [[Christensen and Olson, 2003](#)]. The remaining columns are small
267 scale and highly time dependent. On time average only one column-like feature remains,
268 identified by a strong downwelling somewhat west to the longitude of highest heat flux.

269 The time averaged flows form two main vorticity structures illustrated in figure 10. A
270 long anticyclonic structure associated to the strong equatorial westward flow stretches
271 nearly around the globe and connects the equator with high latitudes inside the tangent
272 cylinder. A smaller cyclonic feature is owed to the eastward equatorial flow.

273 The snapshot and time averaged radial magnetic fields shown in figure 10 are rather
274 similar which demonstrates that the time dependent small scale convective features are
275 not very efficient in creating larger scale coherent magnetic field. The radial field is
276 strongly concentrated in patches above flow downwelling where the associate inflows
277 concentrate the background field [[Olson et al., 1999](#)]. Like in the study for dynamos with

278 homogeneous CMB heat flux by [Aubert et al. \[2008\]](#) the anti-cyclone mainly produces
 279 poloidal magnetic field. The cyclone twists the field in the other direction and therefore
 280 is responsible for the pair of inverse (outward directed here) field patches located at
 281 mid latitudes in the western hemisphere. The exceptional strength of the high latitude
 282 normal flux patches suggests that additional field line stretching further intensified the
 283 field here.

284 3.5 Parameter Dependence

285 Focusing again at the axial heat flux anomaly we further study the influence of Rayleigh
 286 Ra , Ekman E and magnetic Prandtl number Pm . In general we find that, independently
 287 of the Ekman E and Rayleigh numbers Ra , a hemispherical dynamo mode is promoted
 288 once g reaches a value of 60%. Close to the onset of dynamo action a mild variation
 289 can help to maintain dynamo action due to the additional Ω -effect. See the cases at
 290 $E = 10^{-4}$ and either $Ra = 7 \times 10^6$, $Pm = 2$ or $Ra = 2 \times 10^8$, $Pm = 1$ in table 1.
 291 A strong amplitude of the heat flux anomaly can also suppress dynamo action due to
 292 the weakening of convective columns by the Lorentz force. For example, at $E = 10^{-4}$,
 293 $Ra = 4 \times 10^7$ and $Pm = 2$ the dynamo fails once g reaches 200%.

294 Figure 11 shows how the CMB and surface hemisphericity (\mathcal{H}_{cmb} , \mathcal{H}_{sur}) depends
 295 on the magnetic Reynolds number Rm^* based on the equatorially anti-symmetric part
 296 of the zonal flow only and therefore useful to quantify the important Ω -effect in the
 297 hemispherical dynamo cases.

298 For $E = 10^{-4}$ the \mathcal{H}_{cmb} values first increase linearly with Rm^* and then saturates
 299 around $\mathcal{H}_{cmb} \approx 0.75$ for $Rm^* \geq 400$. All cases roughly follow the same curve with the
 300 exception of the peculiar $Ra = 7 \times 10^6$, $Pm = 2$ and $g = 60\%$ case described above.
 301 This means that there is a trade off between g , Ra and Pm ; increasing either parameter
 302 leads to larger Rm^* values. All the solution with hemisphericities $\mathcal{H}_{cmb} > 0.6$ oscillate.

303 The few simulations at smaller Ekman numbers indicate that the degree of hemi-
 304 sphericity decreases with decreasing E . This is to be expected since the Taylor Proud-
 305 man theorem becomes increasingly important [[Landeau and Aubert, 2011](#)], inhibiting
 306 the ageostrophic hemispherical mode. Larger heat flux variation amplitudes can help
 307 to counteract this effect. Since both inertia and Lorentz forces can help to balance the
 308 Coriolis force, increasing either Ra or Pm also helps. For $E = 3 \times 10^{-5}$ an oscillatory
 309 case with $\mathcal{H}_{cmb} = 0.76$ is found for the larger Rayleigh number of $Ra = 4 \times 10^8$ and
 310 $g = 100\%$. For $E = 10^{-5}$ \mathcal{H}_{cmb} remains small at $g = 100\%$ and we could not afford
 311 to increase Ra here since larger Ra as well as lower E values both promote smaller
 312 convective and magnetic length scales and therefore require finer numerical grids.

313 The decrease in length scales has another interesting effect on the radial dependence
 314 of hemisphericity. To yield a maximum hemisphericity, equatorially symmetric ($l +$
 315 $m = \text{even}$) and anti-symmetric ($l + m = \text{odd}$) magnetic field contributions must be
 316 of comparable strength, i.e. obey a 'whitish' spectrum (in a suitable normalization)
 317 [[Grote and Busse, 2000](#)]. Since, however, the radial dependence of the modes depends
 318 on the spherical harmonic degree (they decay like $r^{-(l+2)}$ away from the CMB) the
 319 hemisphericity also depends on radius. The spectrum can only be perfectly 'white' at

320 one radius. The smaller the scale of the magnetic field at r_{cmb} the further this radius
 321 lies beyond r_{cmb} . This explains why the \mathcal{H}_{sur} values shown in the lower panel of figure
 322 11 show a much larger scatter than the \mathcal{H}_{cmb} values. Larger values of Ra , E , but also g
 323 and Pm lead to small magnetic scales and thus larger ratios of \mathcal{H}_{sur} over \mathcal{H}_{cmb} .

324 4 Application to Mars

325 Could the hemispherical dynamo models presented above provide an explanation for
 326 the crustal magnetization found on Mars? To address this question we rely on the
 327 hemisphericity of the crustal magnetization and the magnetic field strength inferred
 328 from Martian meteorites. [Amit et al. \[2011\]](#) use MGS data to estimate a hemisphericity
 329 between $\mathcal{H}_{sur} = 0.45$ and $\mathcal{H}_{sur} = 0.65$. The magnetization of the Martian meteorite
 330 (ALH 84001) suggest a field strength of the ancient dynamo between 5 and 50 μT [[Weiss
 331 et al., 2002](#)].

332 Because our simulations show that the magnetic field strength also varies significantly
 333 with the amplitude of the heat flux pattern, we rescale the dimensionless field strength
 334 in our simulations by assuming that the Elsasser number provides a realistic value.
 335 Assuming a magnetic diffusivity of $\lambda = 1.32 \text{ m}^2 \text{ s}^{-1}$ and density of $\rho = 7000 \text{ kg m}^{-3}$, a
 336 rotation rate of $\Omega = 7.1 \times 10^{-5} \text{ s}^{-1}$ and the magnetic vacuum permeability then allows
 337 to rescale the Elsasser number to dimensional field strengths. Time is rescaled via the
 338 magnetic diffusion time $t_\lambda = D^2 \lambda^{-1}$ with an outer core radius of 1680 km.

339 We have included the Martian crustal hemisphericity values in the lower panel of figure
 340 11 to show that only oscillatory cases fall in the required range with heat flux variation
 341 amplitudes $g \geq 60\%$ and $Rm^* \geq 300$. Figure 12 shows the temporal evolution of \mathcal{H}_{cmb}
 342 and \mathcal{H}_{sur} for one of these cases. The variation is surprisingly strong and oscillates at
 343 twice the frequency of the individual Gauss coefficients. Since all coefficients roughly
 344 oscillate with the same period there are two instances during each period where the
 345 hemisphericity is particularly large (around $\mathcal{H} \approx 0.8$) since axial dipole and quadrupole
 346 have the same amplitude. Since the mean hemisphericity decreases with radius the
 347 variation amplitude is much higher at the planetary surface than at the CMB (figure
 348 12). The strong time dependence of oscillatory cases highlights that considerations over
 349 which period the magnetization was acquired are extremely important.

350 To translate the dynamo field into a magnetization pattern, [Amit et al. \[2011\]](#) suggest
 351 two end-members of how the magnetization was acquired. In the first end-member
 352 scenario called 'random' the crustal magnetization is acquired randomly in time and
 353 space and, according to [Amit et al. \[2011\]](#), should reflect the time averaged intensity.
 354 In the second end-member called 'continuous', magnetization is acquired in global thick
 355 layers, so that the time intensity of the time average field is considered. However,
 356 since the magnetization records the magnetic changes happening during the slow crust
 357 formation, the local net magnetization, as seen by an observer, is always proportional
 358 to the time averaged local magnetic field possibly slightly dominated by the outermost
 359 layers. We therefore think, that the random magnetization scenario does not apply. The
 360 strong magnetization found on Mars indicates that a significant portion of the crust is

361 unidirectionally magnetized. [Langlais et al. \[2004\]](#) estimated a magnetization depth of
362 20 – 40 km depending on the magnetization density. Crust formation is a rather slow
363 process that may take millions of years. Typical magnetic time scales can be much
364 shorter. The periods of the reversing strongly hemispherical dynamos discussed above,
365 amount to not more than about ten thousand years.

366 Table 1 lists the time averaged rescaled magnetic field intensity at the model Martian
367 surface. For $g \leq 60\%$ the field strengths are similar to that predicted for Mars [[Weiss
368 et al., 2002](#)] and fall somewhat below this values for larger g -values. In the strongly
369 hemispherical oscillating cases, however, the amplitude of the time average field average
370 to zero on time scales of the crustal magnetization. We therefore conclude that while the
371 hemispherical dynamos can reach hemisphericities similar to that of the Martian crustal
372 magnetization their oscillatory nature makes them incompatible with the rather strong
373 magnetization amplitude.

374 5 Discussion

375 We find that an equatorially anti-symmetric convective mode is consistently triggered
376 by a cosine heat flux variation that allows more heat to escape through the southern
377 than through the northern outer boundary of the dynamo region. When the variation
378 is strong enough, convective up- and down-wellings are concentrated at the southern
379 hemisphere and the northern hemisphere remains hot. The associated latitudinal tem-
380 perature gradients drive strong thermal winds that dominate the flow when, for example,
381 the variation amplitude g exceeds 50% at $E = 10^4$. Tilting the heat flux pattern axis
382 leaves the solution more or less unchanged with the exception of the 90° -case where
383 the equatorial symmetry remain unbroken. We conclude that breaking the equatorial
384 symmetry is dynamically preferred over an equatorially oriented heat flux anomaly of
385 the CMB heat flux.

386 Due to the thermal winds, the dynamo type changes from α^2 to $\alpha\Omega$ but is generally
387 less efficient. Lorentz forces associated with the toroidal field created via the Ω -effect
388 tend to kill whatever remains of classical columnar convection. This further increases
389 the equatorial anti-symmetry of the solution. Poloidal fields are mainly produced by the
390 southern up- and downwellings which lead to a hemispherical field pattern at the outer
391 boundary.

392 When the hemisphericity approaches values of that found in Martian crustal mag-
393 netization, however, all dynamos start to oscillate on (extrapolated) time scales of the
394 order of 10 kyr. These oscillations are reminiscent of previously described Parker waves
395 in dynamo simulations [[Busse and Simitev, 2006](#)]. As a typical characteristic of Parker
396 waves, the frequency increases with the (square root of the) shear strength, see table
397 1. The oscillation periods are much shorter than the time over which the deep reach-
398 ing Martian magnetization must have been acquired [[Langlais et al., 2004](#)]. Being a
399 composite of many consecutive layers with alternating polarities the net magnetization
400 would scale with the time averaged field and would therefore likely be much smaller
401 than the predicted strength of the ancient Martian field magnetizing the crust [[Weiss](#)

402 [et al., 2002](#)]. The maximum hemisphericity for non-oscillatory dynamos amounts to a
403 configuration where the mean northern field amplitude is only 50% weaker than the
404 southern. Additional effects like lava-overflows would then be required to explain the
405 observed hemisphericity.

406 [Amit et al. \[2011\]](#), [Stanley et al. \[2008\]](#) also studied the effects of the identical sinusoidal
407 boundary heat flux pattern and find very similar hemispherical solutions. [Amit et al.](#)
408 [\[2011\]](#) used a very similar setup to ours and also reported oscillations when the dynamo
409 becomes strongly hemispherical. [Stanley et al. \[2008\]](#) do not report the problematic
410 oscillations intensively studied here, which may have to do with differences in the dynamo
411 models. They study stress-free rather than rigid flow boundaries and assume that the
412 growing inner core contributes to drive the dynamo while our model exclusively relies
413 on internal heating. Should a hemispherical dynamo indeed be required to explain the
414 observed magnetization dichotomy, this may indicate that ancient Mars already had
415 an inner core. Alternatively efficient demagnetization mechanisms may have modified
416 an originally more or less homogeneous magnetized crust [[Shahnas and Arkani-Hamed,](#)
417 [2007](#)].

418 [Landeau and Aubert \[2011\]](#) observed that similar hemispherical dynamos are found
419 when the Rayleigh number exceeds a critical value. However, albeit the effects are
420 significantly smaller than when triggered via the boundary heat flux. All the cases
421 explored here remain below this critical Rayleigh number. [Landeau and Aubert \[2011\]](#)
422 also mentioned that the equatorial anti-symmetry, and thus the hemisphericity of the
423 magnetic field, decreases when the Ekman number is decreased. Our simulations at
424 lower Ekman number seem to confirm this trend although a meaningful extrapolation to
425 the Martian value of $E = 3 \times 10^{-15}$ would require further simulations at lower Ekman
426 numbers. To a certain extent the decrease can be compensated by increasing the heat
427 flux variation amplitude, the Rayleigh number or the magnetic Prandtl number.

428 Our results show that a north-south symmetry breaking induced by lateral CMB
429 heat flux variations can yield surprisingly strong effects. Fierce thermal winds and
430 local southern upwellings take over from classical columnar convection and the dynamo
431 changes from an α^2 to an $\alpha\Omega$ -type. The dominant Ω -effect seems always linked to
432 Parker-wave-like field oscillations typically discussed for stellar applications. It will be
433 interesting to further explore the aspects independent of the application to Mars.

434 **Acknowledgments**

435 The authors thank Ulrich Christensen for helpful discussions. W. Dietrich acknowledges
436 a PhD fellowship from the Helmholtz Research Alliance 'Planetary Evolution and Life'
437 and support from the 'International Max Planck Research School on Physical Processes
438 in the Solar System and Beyond'.

439 References

- 440 M. H. Acuña, J. E. P. Connerney, N. F. Ness, R. P. Lin, D. Mitchell, C. W. Carlson,
441 J. McFadden, K. A. Anderson, H. Reme, C. Mazelle, D. Vignes, P. Wasilewski, and
442 P. Cloutier. Global Distribution of Crustal Magnetization Discovered by the Mars
443 Global Surveyor MAG/ER Experiment. *Science*, 284:790–793, April 1999. doi: 10.
444 1126/science.284.5415.790.
- 445 M. H. Acuña, J. E. P. Connerney, P. Wasilewski, R. P. Lin, D. Mitchell, K. A. Anderson,
446 C. W. Carlson, J. McFadden, H. Rème, C. Mazelle, D. Vignes, S. J. Bauer, P. Cloutier,
447 and N. F. Ness. Magnetic field of Mars: Summary of results from the aerobraking and
448 mapping orbits. *Journal of Geophysical Research*, 106:23403–23418, October 2001.
449 doi: 10.1029/2000JE001404.
- 450 H. Amit and P. Olson. Time-average and time-dependent parts of core flow. *Physics of*
451 *the Earth and Planetary Interiors*, 155:120–139, April 2006. doi: 10.1016/j.pepi.2005.
452 10.006.
- 453 H. Amit, U. R. Christensen, and B. Langlais. The influence of degree-1 mantle hetero-
454 geneity on the past dynamo of Mars. *Physics of the Earth and Planetary Interiors*,
455 189:63–79, November 2011. doi: 10.1016/j.pepi.2011.07.008.
- 456 J. Arkani-Hamed and P. Olson. Giant impact stratification of the Martian core. *Geo-*
457 *physical Research Letters*, 37:2201–2205, January 2010. doi: 10.1029/2009GL041417.
- 458 J. Aubert, J. Aurnou, and J. Wicht. The magnetic structure of convection-driven nu-
459 merical dynamos. *Geophysical Journal International*, 172:945–956, March 2008. doi:
460 10.1111/j.1365-246X.2007.03693.x.
- 461 J. Aubert, S. Labrosse, and C. Poitou. Modelling the palaeo-evolution of the geodynamo.
462 *Geophysical Journal International*, 179:1414–1428, December 2009. doi: 10.1111/j.
463 1365-246X.2009.04361.x.
- 464 J. Bloxham. Sensitivity of the geomagnetic axial dipole to thermal core-mantle interac-
465 tions. *Nature*, 405:63–65, May 2000.
- 466 S. I. Braginsky and P. H. Roberts. Equations governing convection in earth’s core and
467 the geodynamo. *Geophysical and Astrophysical Fluid Dynamics*, 79:1–97, 1995. doi:
468 10.1080/03091929508228992.
- 469 D. Breuer, S. Labrosse, and T. Spohn. Thermal Evolution and Magnetic Field Gener-
470 ation in Terrestrial Planets and Satellites. *Space Science Reviews*, 152:449–500, May
471 2010. doi: 10.1007/s11214-009-9587-5.
- 472 F. H. Busse and R. D. Simitsev. Parameter dependences of convection-driven dynamos
473 in rotating spherical fluid shells. *Geophysical and Astrophysical Fluid Dynamics*, 100:
474 341–361, October 2006. doi: 10.1080/03091920600784873.

- 475 U. R. Christensen and P. Olson. Secular variation in numerical geodynamo models with
476 lateral variations of boundary heat flow. *Physics of the Earth and Planetary Interiors*,
477 138:39–54, June 2003. doi: 10.1016/S0031-9201(03)00064-5.
- 478 U. R. Christensen, J. Aubert, and P. Olson. Convection-driven planetary dynamos. In
479 T. Kuroda, H. Sugama, R. Kanno, & M. Okamoto, editor, *IAU Symposium*, volume
480 239 of *IAU Symposium*, pages 188–195, May 2007. doi: 10.1017/S1743921307000403.
- 481 J. E. P. Connerney, M. H. Acuña, P. J. Wasilewski, G. Kletetschka, N. F. Ness, H. Rème,
482 R. P. Lin, and D. L. Mitchell. The Global Magnetic Field of Mars and Implications
483 for Crustal Evolution. *Geophysical Research Letters*, 28:4015–4018, November 2001.
484 doi: 10.1029/2001GL013619.
- 485 G. Dreibus and H. Wänke. Mars, a volatile-rich planet. *Meteoritics*, 20:367–381, June
486 1985.
- 487 G. A. Glatzmaier, R. S. Coe, L. Hongre, and P. H. Roberts. The role of the Earth’s
488 mantle in controlling the frequency of geomagnetic reversals. *Nature*, 401:885–890,
489 October 1999. doi: 10.1038/44776.
- 490 E. Grote and F. H. Busse. Hemispherical dynamos generated by convection in rotating
491 spherical shells. *Physical Review E*, 62:4457–4460, September 2000. doi: 10.1103/
492 PhysRevE.62.4457.
- 493 H. Harder and U. R. Christensen. A one-plume model of martian mantle convection.
494 *Nature*, 380:507–509, April 1996. doi: 10.1038/380507a0.
- 495 K. Hori, J. Wicht, and U. R. Christensen. The effect of thermal boundary conditions
496 on dynamos driven by internal heating. *Physics of the Earth and Planetary Interiors*,
497 182:85–97, September 2010. doi: 10.1016/j.pepi.2010.06.011.
- 498 T. Keller and P. J. Tackley. Towards self-consistent modeling of the martian dichotomy:
499 The influence of one-ridge convection on crustal thickness distribution. *Icarus*, 202:
500 429–443, August 2009. doi: 10.1016/j.icarus.2009.03.029.
- 501 C. Kutzner and U. Christensen. Effects of driving mechanisms in geodynamo models.
502 *Geophysical Research Letters*, 27:29–32, 2000. doi: 10.1029/1999GL010937.
- 503 C. Kutzner and U. R. Christensen. Simulated geomagnetic reversals and preferred virtual
504 geomagnetic pole paths. *Geophysical Journal International*, 157:1105–1118, June 2004.
505 doi: 10.1111/j.1365-246X.2004.02309.x.
- 506 M. Landeau and J. Aubert. Equatorially asymmetric convection inducing a hemispherical
507 magnetic field in rotating spheres and implications for the past martian dynamo.
508 *Physics of the Earth and Planetary Interiors*, 185:61–73, April 2011. doi: 10.1016/j.
509 pepi.2011.01.004.

- 510 B. Langlais, M. E. Purucker, and M. Mandea. Crustal magnetic field of Mars. *Journal of Geophysical Research (Planets)*, 109:E02008, February 2004. doi: 10.1029/
511 2003JE002048.
- 513 R. J. Lillis, H. V. Frey, and M. Manga. Rapid decrease in Martian crustal magnetization
514 in the Noachian era: Implications for the dynamo and climate of early Mars. *Geo-*
515 *physical Research Letters*, 35:14203–14209, July 2008. doi: 10.1029/2008GL034338.
- 516 P. S. Mohit and J. Arkani-Hamed. Impact demagnetization of the martian crust. *Icarus*,
517 168:305–317, April 2004. doi: 10.1016/j.icarus.2003.12.005.
- 518 A. Morschhauser, M. Grott, and D. Breuer. Crustal recycling, mantle dehydration, and
519 the thermal evolution of Mars. *Icarus*, 212:541–558, April 2011. doi: 10.1016/j.icarus.
520 2010.12.028.
- 521 P. Olson, U. Christensen, and G. A. Glatzmaier. Numerical modeling of the geodynamo:
522 Mechanisms of field generation and equilibration. *Journal of Geophysical Research*,
523 1041:10383–10404, May 1999. doi: 10.1029/1999JB900013.
- 524 E. N. Parker. Hydromagnetic Dynamo Models. *Astrophysical Journal*, 122:293, Septem-
525 ber 1955. doi: 10.1086/146087.
- 526 C. C. Reese and V. S. Solomatov. Early martian dynamo generation due to giant impacts.
527 *Icarus*, 207:82–97, May 2010. doi: 10.1016/j.icarus.2009.10.016.
- 528 J. H. Roberts and S. Zhong. Degree-1 convection in the Martian mantle and the origin
529 of the hemispheric dichotomy. *Journal of Geophysical Research (Planets)*, 111:6013–
530 6035, June 2006. doi: 10.1029/2005JE002668.
- 531 J. H. Roberts, R. J. Lillis, and M. Manga. Giant impacts on early Mars and the cessation
532 of the Martian dynamo. *Journal of Geophysical Research (Planets)*, 114:4009–4019,
533 April 2009. doi: 10.1029/2008JE003287.
- 534 G. Schubert and T. Spohn. Thermal history of Mars and the sulfur content of its
535 core. *Journal of Geophysical Research*, 95:14095–14104, August 1990. doi: 10.1029/
536 JB095iB09p14095.
- 537 H. Shahnas and J. Arkani-Hamed. Viscous and impact demagnetization of Martian
538 crust. *Journal of Geophysical Research (Planets)*, 112:E02009, February 2007. doi:
539 10.1029/2005JE002424.
- 540 S. Stanley, L. Elkins-Tanton, M. T. Zuber, and E. M. Parmentier. Mars’ Paleomag-
541 netic Field as the Result of a Single-Hemisphere Dynamo. *Science*, 321:1822–1824,
542 September 2008. doi: 10.1126/science.1161119.
- 543 D. J. Stevenson, T. Spohn, and G. Schubert. Magnetism and thermal evolution of the
544 terrestrial planets. *Icarus*, 54:466–489, June 1983. doi: 10.1016/0019-1035(83)90241-5.

- 545 B. P. Weiss, H. Vali, F. J. Baudenbacher, J. L. Kirschvink, S. T. Stewart, and D. L.
546 Shuster. Records of an ancient Martian magnetic field in ALH84001. *Earth and*
547 *Planetary Science Letters*, 201:449–463, August 2002. doi: 10.1016/S0012-821X(02)
548 00728-8.
- 549 J. Wicht. Inner-core conductivity in numerical dynamo simulations. *Physics of the Earth*
550 *and Planetary Interiors*, 132:281–302, October 2002.
- 551 M. Yoshida and A. Kageyama. Low-degree mantle convection with strongly temperature-
552 and depth-dependent viscosity in a three-dimensional spherical shell. *Journal of*
553 *Geophysical Research (Solid Earth)*, 111:3412–3422, March 2006. doi: 10.1029/
554 2005JB003905.

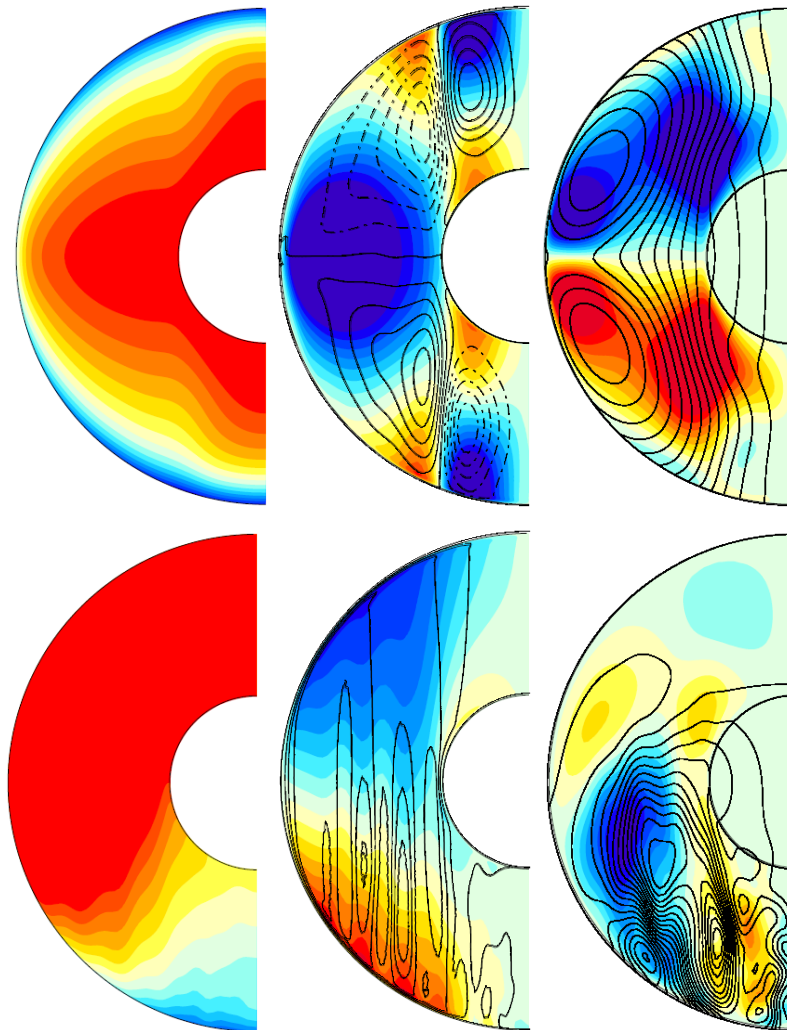


Figure 1: Zonal average of the temperature (left plots), zonal flow with meridional circulation contours (middle plots) and toroidal field with poloidal field line contours (right plots) for columnar convection dominated and magnetic dipolar reference case (left) and a typical hemispherical dynamo solution with the strong EAA symmetry in the flow (right). See the online-version of the article for the color figure.

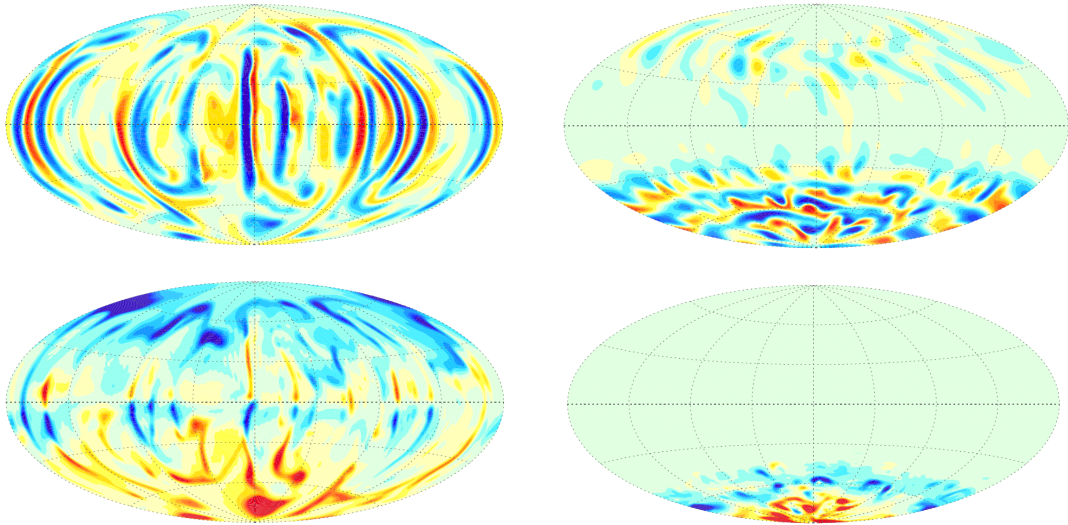


Figure 2: Radial flow (top row) at mid-depth and radial field at CMB (lower row) for the columnar reference case (left) and the hemispherical dynamo (right), indicates the reduction of the magnetic signature at the CMB if the radial motions are limited to the southern polar cusp of high heat flux. Here an Aitoff projection of the spherical CMB is used. See the online-version of the article for the color figure.

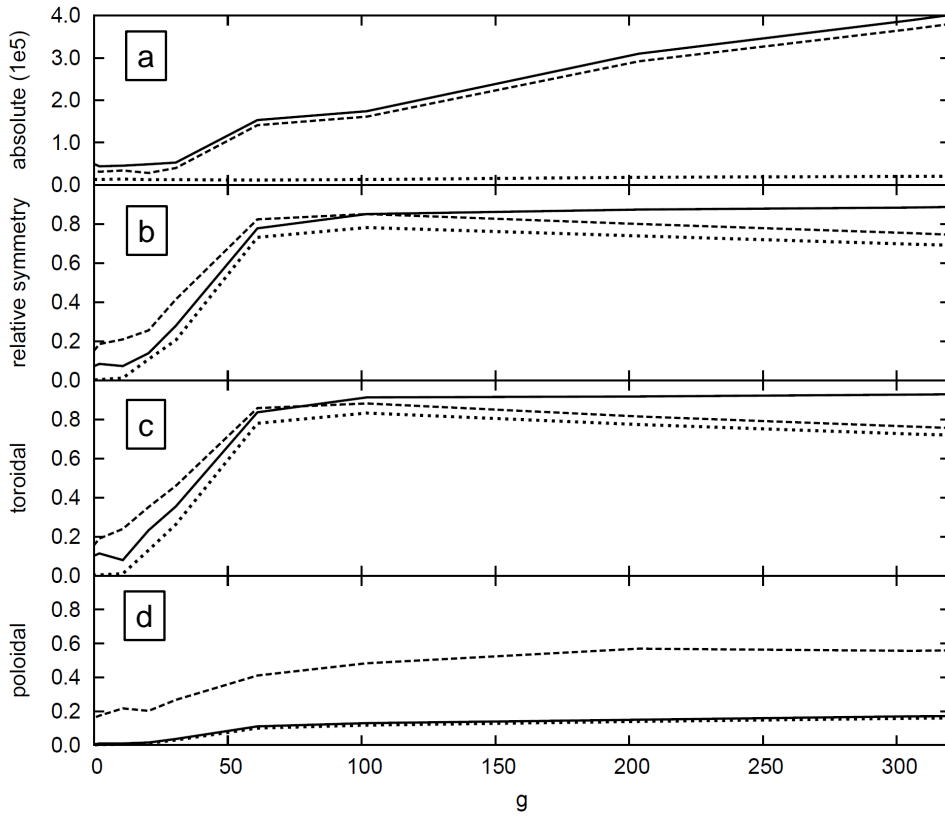


Figure 3: Symmetries and amplitude of total kinetic energy and toroidal/poloidal contributions as a function of g . a) total (solid line), toroidal (dashed) and poloidal (dotted) kinetic energy; b) relative amount of axisymmetry (solid), equatorial anti-symmetry (dashed) and the combined symmetries (EAA, dotted) of the full kinetic energy; c) and d) show the same but separated into toroidal and poloidal contributions.

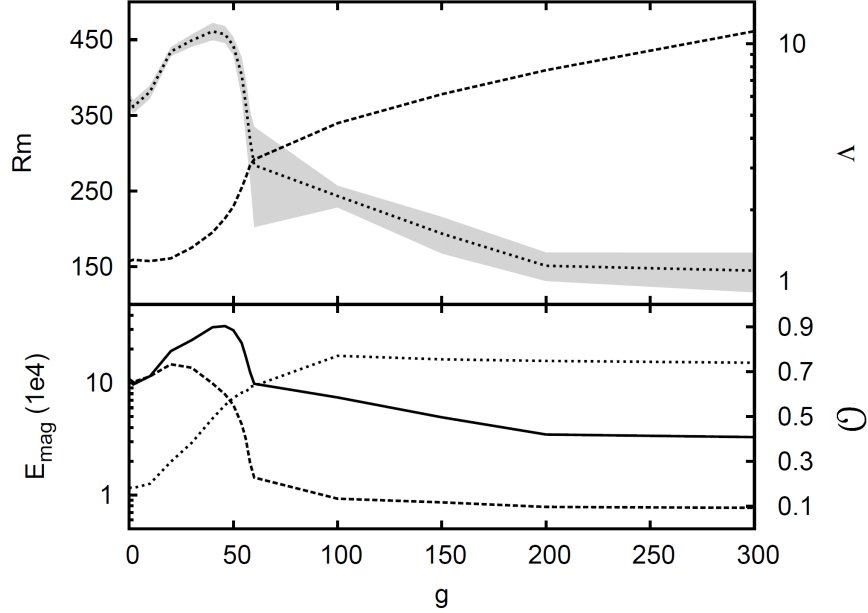


Figure 4: Upper panel: Flow amplitude in terms of the magnetic Reynolds number (solid line) and magnetic field strength in terms of Elsasser number (dashed)) as function of the CMB heat flux anomaly amplitude g , shows the difference between both dynamo regimes in the efficiency of inducing a dynamo. The hemispherical solution, with the $\alpha\Omega$ -induction contains large amounts of axisymmetric zonal flows created by the Coriolis force, therefore the kinetic energy is drastically larger than in the columnar regime ($g = 0$). The magnetic energy decreases, the more the g increases. The gray shade correspond to the standard deviation due to time variability.

Lower panel: Toroidal (dashed) and poloidal (solid) magnetic field in nondimensional units and the relative Ω -effect in terms of Θ (dotted) as a function of g demonstrates the transformation of induction characteristic from an α^2 -dynamo at $g = 0$ (columnar dynamo) towards an $\alpha\Omega$ -type from $g = 60\%$ (hemispherical solution).

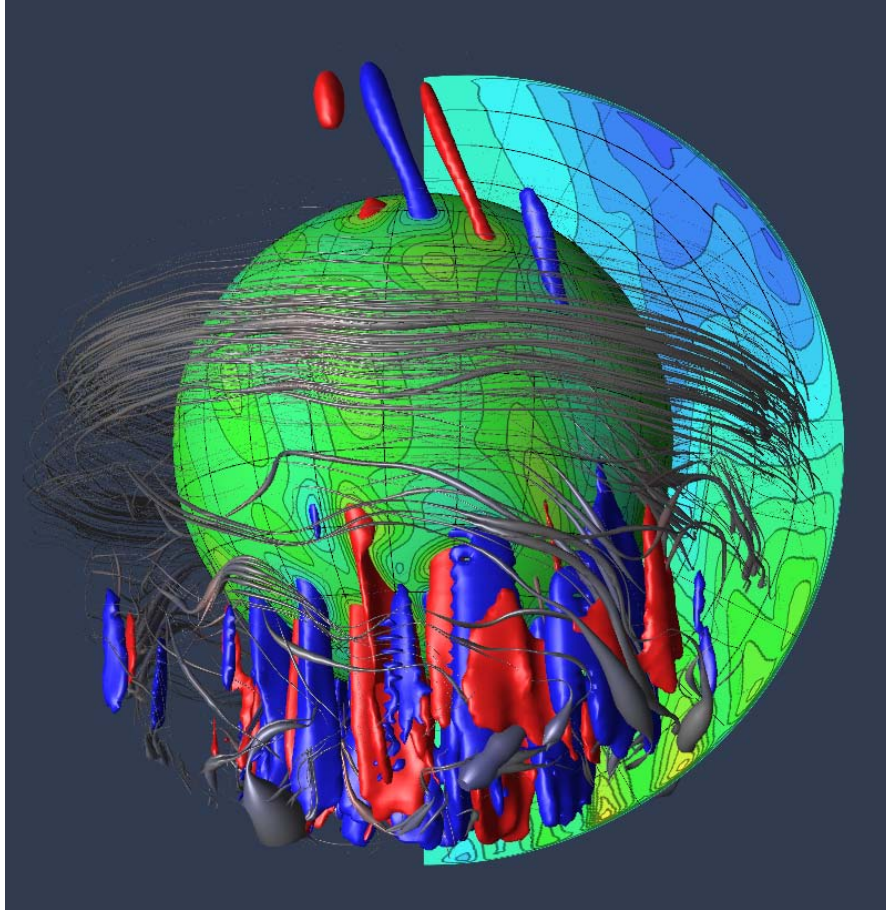


Figure 5: 3D visualization of flow and magnetic field generation in a hemispherical dynamo. The meridional cut depicts contours of axisymmetric zonal flows with prograde (retrograde) directions shown in yellow/red (blue). Outward (inward) radial flows are shown as yellow/red (blue) contours of a spherical shell at mid depth $r_{icb} + (r_{cmb} - r_{icb})/2$. Red (blue) isosurfaces depict the 3D structure of convective upwellings (downwellings). Gray fieldlines illustrate the magnetic field configuration. Their thickness is scaled with the local magnetic field energy. See the article online-version for the color figure.

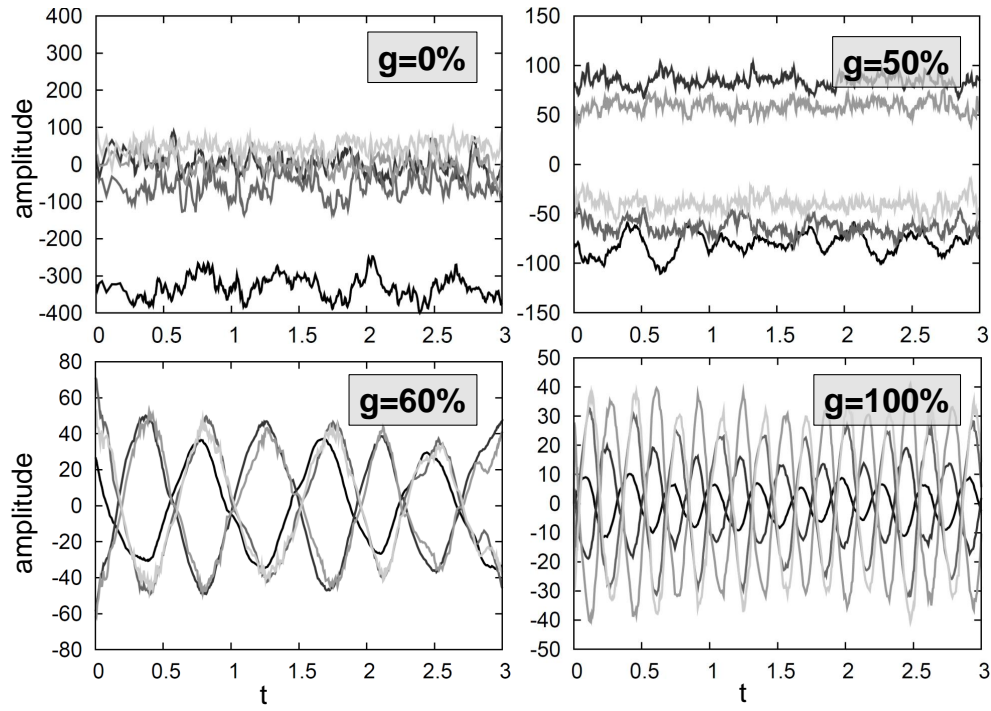


Figure 6: Time evolution of the first five axisymmetric Gauss coefficients at the CMB for the dipole dominated ($g = 0\%, 50\%$) (first and second panel), the oscillatory ($g = 60\%$, third panel) and the reversing hemispherical regime ($g = 100\%$ bottom). The colours indicate different spherical harmonic degrees l : black $l = 1$, dark gray $l = 2$, gray $l = 3$, light gray $l = 4$, faint gray $l = 5$.

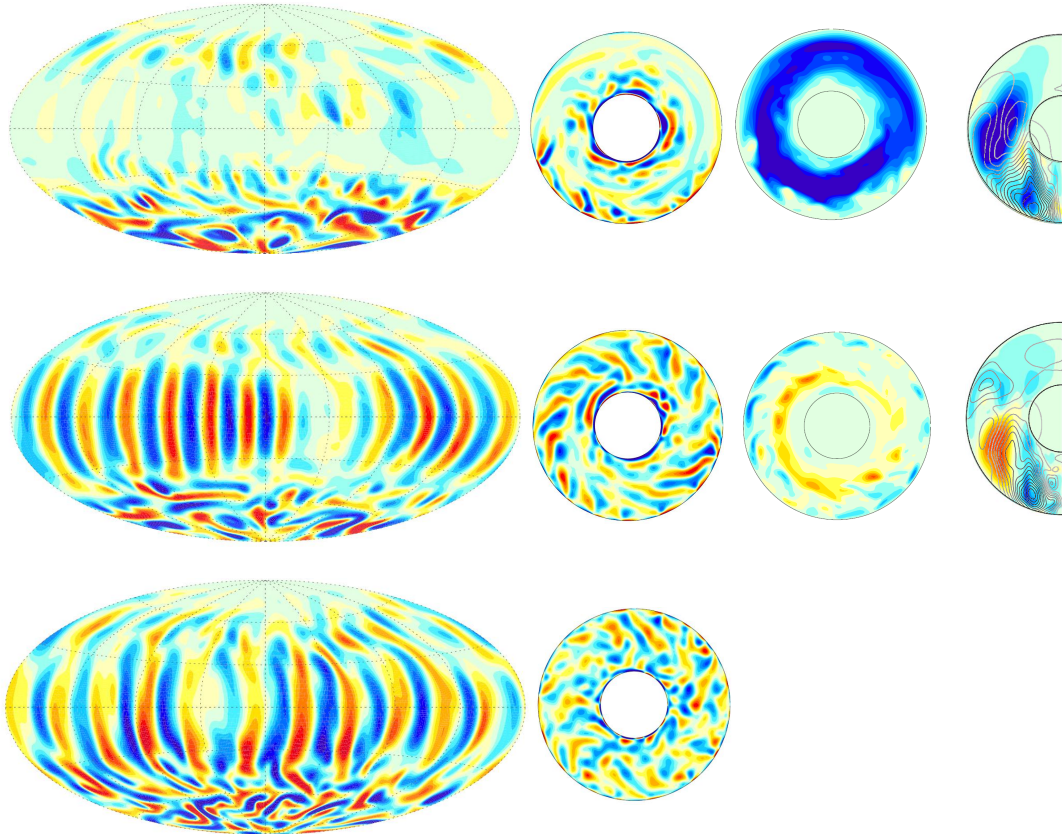


Figure 7: The upper two rows depict the solution at $g = 60\%$ at maximum ($\Lambda = 12$) and minimum magnetic field amplitude ($\Lambda = 0.06$) respectively. The lower row shows a non-magnetic simulation at identical parameters for comparison. Each row shows from left to right: the radial flow at mid depth in the shell, the z-vorticity in the equatorial plane, the azimuthal magnetic field at the equator and the zonal toroidal field. See the online-version of the article for the color figure.

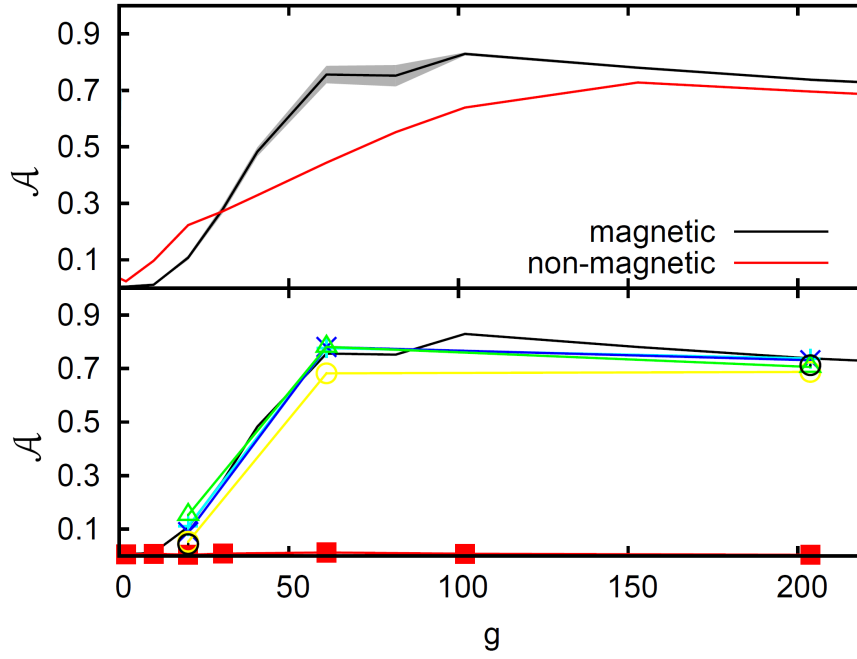


Figure 8: upper panel : Effect of the Lorentz force on the relative kinetic energy in the EAA mode for dynamo (black) and non-magnetic (gray) simulations. The time variability is indicated by gray shaded areas in the width of the standard deviation. The magnetic oscillation described in the text lead to the stronger time variability in the dynamo simulations at $g = 60\%$ and $g = 100\%$. lower panel: The relative equatorially anti-symmetric and axisymmetric energy for different tilting angles follows the onset of EAA convective mode in the case for the axial pattern (black line). For the equatorial orientation (squares) the EAA contribution to total kinetic energy remains Zero. Triangles - 10° , crosses - 30° , faint circles- 45° , dark circles - 60° , plus symbols - 80° . See the online-version of the article for the color figure.

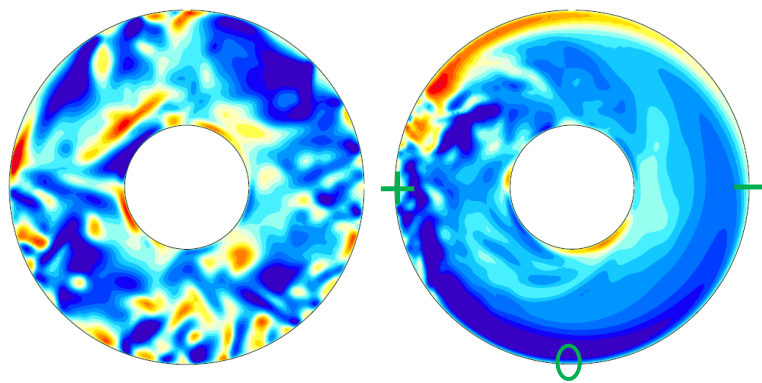


Figure 9: Equatorial slice of u_ϕ for the homogeneous reference case (left) and the equatorial heat flux anomaly (right). The plus, minus and zero character describe the maximal, minimal and the zero line of the anomaly. See the online-version of the article for the color figure.

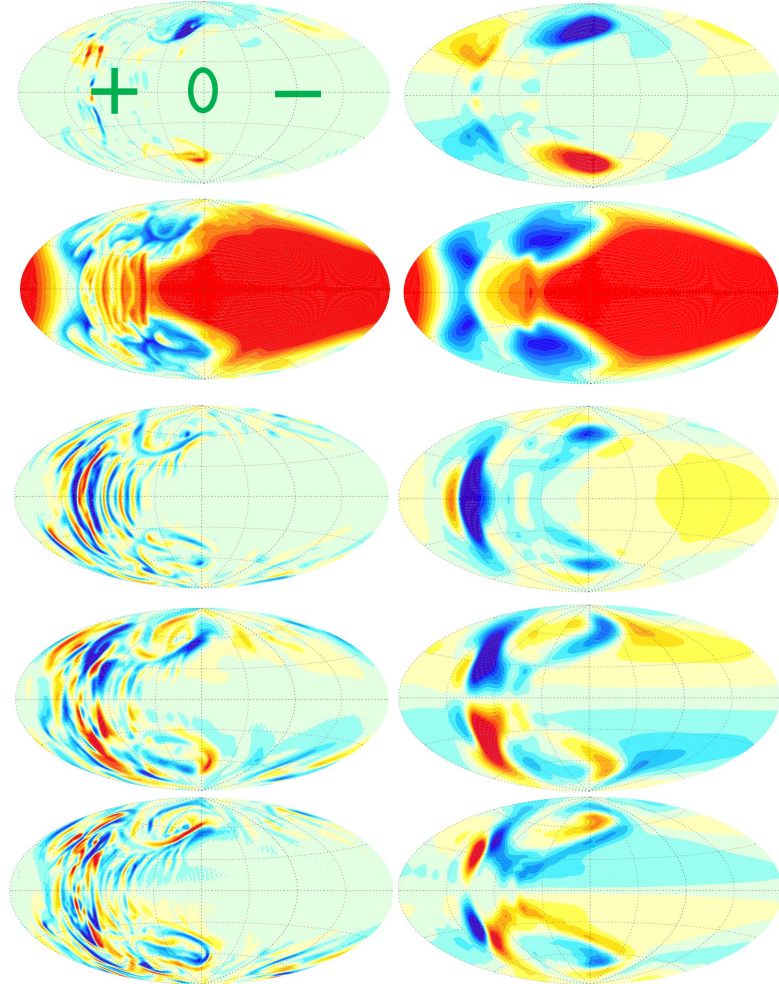


Figure 10: Aitoff projections of spherical surfaces of (from top to bottom) radial field, temperature (both at the CMB), u_r , u_θ and z -vorticity at $r/r_{cmb} = 0.8$ for a snapshot (left plots) and the time average (right). Parameters: $Ra = 4 \times 10^7$, $E = 10^{-4}$, $Pm = 2$, equatorial ($l = m = 1$) perturbation with $g = 100\%$ relative amplitude. See the online-version of the article for the color figure.

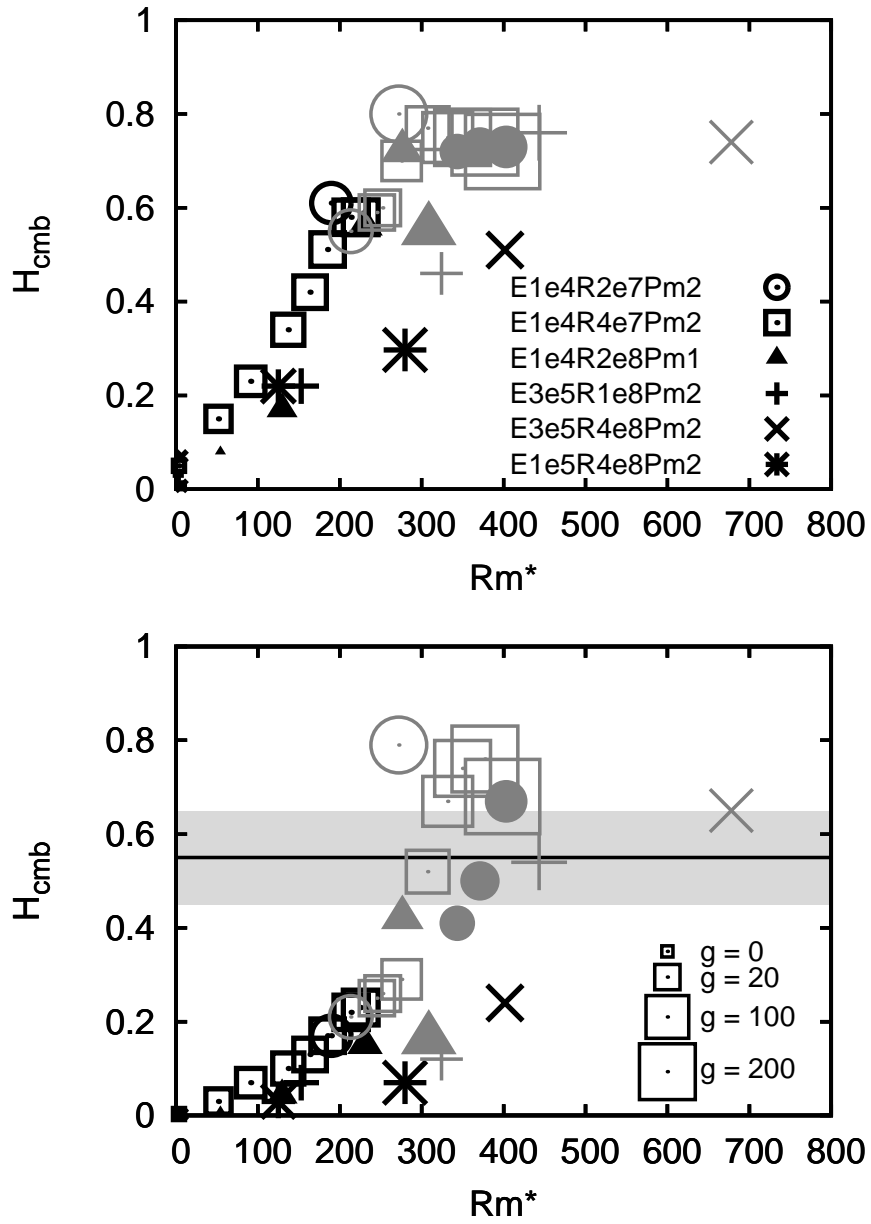


Figure 11: Top panel: Hemisphericity at CMB versus Rm^* , the magnetic Reynolds number based on the equatorially anti-symmetric thermal wind. Oscillatory dynamos in gray, stationary in black symbols.
 bottom panel: Hemisphericity at the (imaginary) Martian surface versus Rm^* .

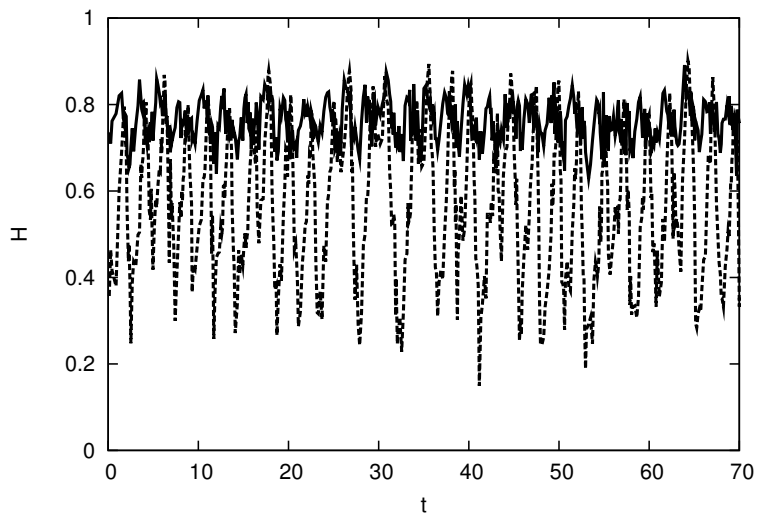


Figure 12: Time evolution of hemisphericity \mathcal{H} at the CMB (solid) and surface (dashed) for $g = 100\%$, $Ra = 4 \times 10^7$, $E = 10^{-4}$ and $Pm = 2$.